RESEARCH PAPER

The influence of aging times at 650 °C on the microstructure of dissimilar laser welded joints of GH159/GH4169 superalloy

Dan Zhao[1,2,3] · Qian Ran[1,2,3] · Song Xiang[1,2,3] · Shuang Hu[1,2,3] · Yuanbiao Tan[1,2,3] · Wei Shi[1,2,3]

Abstract

This study explored the aging time-dependent microstructures and strengthening mechanisms of dissimilar welds between GH159 and GH4169 superalloy. The joint consisted of γ-Ni matrix, nano-scale γ′ and γ″ phases, granular MC carbides, and Laves phase after welding and aging at 650 °C. The aging time mainly affects the precipitation, size, and transformation of the strengthening phase. The weld joints aged for short times (≤ 25 h); the content of small-sized strengthening phases γ′ and γ″ increased gradually with the increased aging time. It can increase the microhardness of the weld center from 252 HV (unaged) to 396 HV (aged for 25 h). With a longer aging time (≥ 600 h), the Laves phase produced during welding and the nano-scale phases precipitated by aging are severely coarsened. With increasing aging time to 2000 h, the nano-scale phase γ′ increasingly transforms into the δ phase, resulting in its performance degradation. However, the δ phase has the effect of "cutting" the Laves phase, which can refine the Laves to a certain extent.

Keywords Post-weld aging treatment · Laves phases · γ′ phase · Microhardness

1 Introduction

Bolt connection is one of the most important and key connection types in aero-engine combined rotor system. Its main function is to connect the turbine disc and shaft [1–3]. A superalloy is comprehensively used in high-pressure rotor bolts because of its outstanding mechanical properties at high temperatures, excellent fatigue properties, and good oxidation resistance [4–7]. Generally, it is usually composed of spring plates and bolts, and the long-term connection of

---

✉ Song Xiang
  sxiang@gzu.edu.cn

✉ Yuanbiao Tan
  ybtan1@gzu.edu.cn

1 College of Materials and Metallurgy, Guizhou University, Guiyang 550025, China

2 Key Laboratory for Mechanical Behavior and Microstructure of Materials of Guizhou Province, Guiyang 550025, China

3 National & Local Joint Engineering Laboratory for High-Performance Metal Structure Material and Advanced Manufacturing Technology, Guiyang 550025, China

the two parts is widely made by laser beam welding (LBW) [8–10].

In order to lessen the machining costs and improve the service life and performance of the bolted connection assembly, a different combination of superalloys has been considered for using in high-pressure rotor bolt welding. For instance, GH4169 superalloy is preferred at higher temperatures (~ 650 °C) [11–13], while GH159 superalloy is used at lower temperatures (~ 595 °C) [14, 15]. Both superalloys exhibit superior corrosion resistance at high temperatures attributing to the existence of chromium, while the GH159 superalloy is more advantageous owing to its higher strength [16–18]. Therefore, dissimilar metal welding (DMW) of GH4169 and GH159 superalloys is a promising option for processing high-pressure rotor bolts. However, DMW complicates the microstructure and mechanical properties of the weldments. Ran et al. [19] reported that the macroscopic morphology of the weld can be effectively improved and the joint performance of GH4169 and GH159 superalloys can be improved by adjusting the welding parameters. The authors observed the existence of the eutectic Laves phase in the center of the weld, and its precipitation would consume strengthening elements, thereby reducing the mechanical properties of the joints. Furthermore, it is difficult to obtain high-quality joints with DMW of GH4169 and GH159

Table 1 The chemical compositions of GH4169 and GH159 superalloy (wt %)

| elements	Ni	Co	Cr	Fe	Nb	Mo	Ti	Al	C
GH4169	51.25	0.03	17.91	21.61	4.89	2.96	0.80	0.52	0.03
GH159	25.5	35.5	19	9	0.6	7	3	0.2	

superalloys because of variations in their material properties such as chemical composition, thermal conductivity, and thermal expansion coefficients. For example, dissimilar materials can generate severe elemental segregation during welding and lead to uneven distribution of precipitates.

All the welding processes give rise to composition segregation at the weld joints owing to different chemical compositions and thermal expansion coefficients of DMW. Many researchers [20–24] reported that post-weld heat treatment is an inevitable step for alleviating composition segregation and stabilizing the microstructure of the weldment. Wang et al. [25] confirmed that the aging treatment process contributed to precipitating a large amount of γ′ phases, and the existence of γ′ phase with bimodal size could significantly enhance the strength of IN718 superalloy. Zhou et al. [26] found that the gradient grain is formed in the weld of GH4169 superalloy after post-welding heat treatment, which can effectively alleviate strain concentration and promote the accumulation of more dislocations. Finally, the ductility was increased by 16.57% compared to the samples under the identical treatment, and the strength was not lost. Damodaram et al. [27] have found that post-welding aging promoted the precipitation of the strengthened phase and was beneficial to improve the tensile property of the weld of IN718 superalloy.

As a result, post-welding heat treatment is an essential means to restore the excellent mechanical properties of joints by adjusting the morphology, distribution, and quantity of various precipitates. However, there are very few literature reports on the effect of post-welding aging treatment on welded joints of GH4169 and GH159 superalloys. The characteristics and interrelations of weld appearances, microstructure evolution, and mechanical properties of the weldment under post-welding aging treatment conditions are still unclear. The research of this paper is mainly to provide some references for these problems.

2 Materials and methods

The leaf spring and bolt materials used in this experiment are GH4169 and GH159 superalloys, respectively. Its chemical composition is shown in Table 1. Before laser beam welding (LBW), the GH4169 and GH159 superalloys are heat treated under different conditions, respectively. For GH4169 superalloy, the solution treatment was conducted at 1050 °C for 2 h and then air-cooled to room temperature.
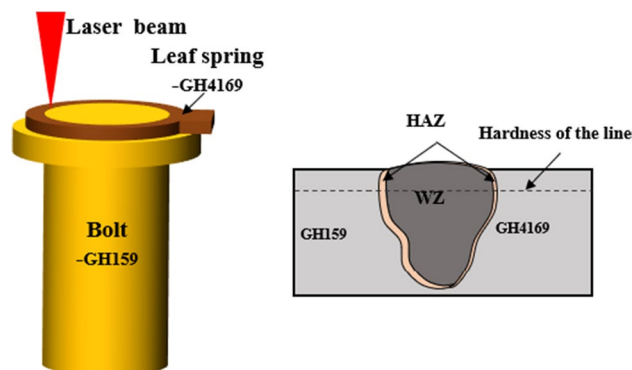
Fig. 1 Schematic diagram of laser welded joint of dissimilar superalloy

Table 2 Operation parameters for laser welding of GH4169 and GH159 superalloy

Laser power (watt)	Welding speed (mm/s)	Protection gas flow (L/h)		Heat input (J/mm)
528	15	500	35.2	

Afterward, double-aging treatment (720 °C × 8 h/furnace cooling followed by 620 °C × 8 h/air cooling) is carried out in the solution-treated GH4169 superalloy. For GH159 superalloy, the samples were solution annealed at 1025 °C for 4 h before the welding and then air-cooled to room temperature. Subsequently, the solution-treated samples were cold-drawn to a strain of 48% by multi-pass and then were hot pier. Figure 1 shows the schematic diagram of the welded joint, and the microstructure of different areas in the welded joint is observed. The equipment used in the connection bolt laser welding is CF-1000 continuous laser welding machine, and argon gas serves as the protective gas during the whole welding process. Table 2 shows the welding parameters used in this study. Post-welding heat treatment is performed on GH159 and GH4169 superalloy joints at 650 °C for 25, 600, and 2000 h.

The samples were polished employing prescriptive metallographic preparation methods, which were etched in a solution of 5 g $CuSO_4$ + 100 ml HCl + 5 ml H_2SO_4. The microstructures of the specimen were observed by using optical microscopy (OM) selected Olympus GX51, a thermal field emission scanning electron microscope (SEM) and EDS analyzer with OXFORD energy spectrum, and transmission

electron microscopy (TEM) with an accelerating voltage of 200 kV (FEI Talos F200X). The microhardness value of the welded joint in all areas was measured by the HVS-1000 Vickers microhardness employing a load of 1000 g for 10 s, and the test is no less than three times to ensure the accuracy of hardness values. The size and volume fraction of all precipitates were measured by the Image-Pro Plus (IPP) analysis software.

3 Results and discussions

3.1 Microstructure of the weld

The microstructure of the weld joint of GH159/GH4169 superalloy is shown in Fig. 2a, which shows a stemless wine cup shape without defects such as metal spatter and non-fusion. However, it is unavoidable to observe the presence of porosity at the bottom of the weld. The presence of porosity is mainly related to the high Ni content in the base metal (BM) [28]. As is shown in Fig. 2b, the microstructure and properties of solid BM on both sides of the weld significantly change under the action of the welding thermal cycle, forming a heat-affected zone (HAZ) [29, 30]. The dashed line near the center of the weld is the fusion line, and the dashed line near the BM is the HAZ boundary. The weld zone (WZ) is the high-temperature concentrated melting zone of the fusion welding heat source. Presented in Fig. 2c is the microstructure of the weld joint from left to right, followed by GH159BM, GH159 heat-affected zone (GH159HAZ), weld, GH4169 heat-affected zone (GH4169HAZ), and GH4169BM. The center structure of the weld is fine equiaxed crystals, and the edge of the weld is a dendrite region. The dendrites grow along the vertical direction of the solid–liquid interface; that is, the vertical fusion line grows toward the center of the weld. Based on the fast heat dissipation at the edge, the grains near the fusion line grow the fastest and are mainly coarse dendrites [31,

32]. Due to the difference in melting temperature between the two superalloys, the width of HAZ zone on both sides is different. The width of the HAZ formed after welding is determined by the physical properties of the material, such as melting point, thermal conductivity, and thermal expansion coefficient. In addition, the width of heat-affected zone is also related to welding parameters (such as welding power and speed). By comparison, it can be observed that the low-strength GH4169 superalloy has a wider liquefaction region; this phenomenon has been mentioned in previous studies by Moosavy et al. [33].

3.2 Microhardness

Figure 3 exhibits the microhardness profile of the weldments and the corresponding microhardness values are listed in Table 3. The welding center is often regarded as the weakest link of the assembly. The failure of GH159 and GH4169 superalloy welds mostly originates from the weld
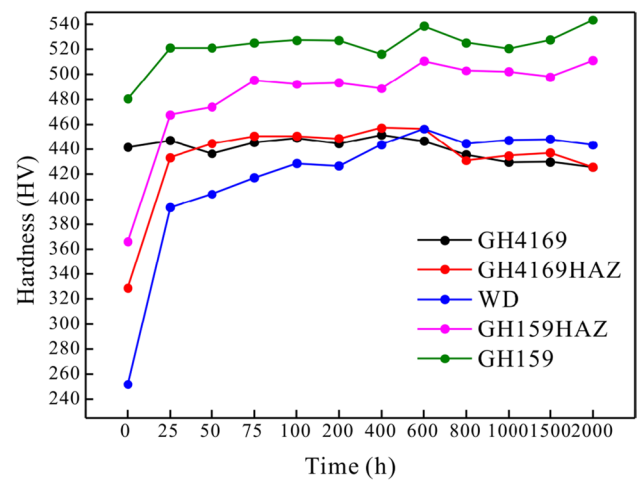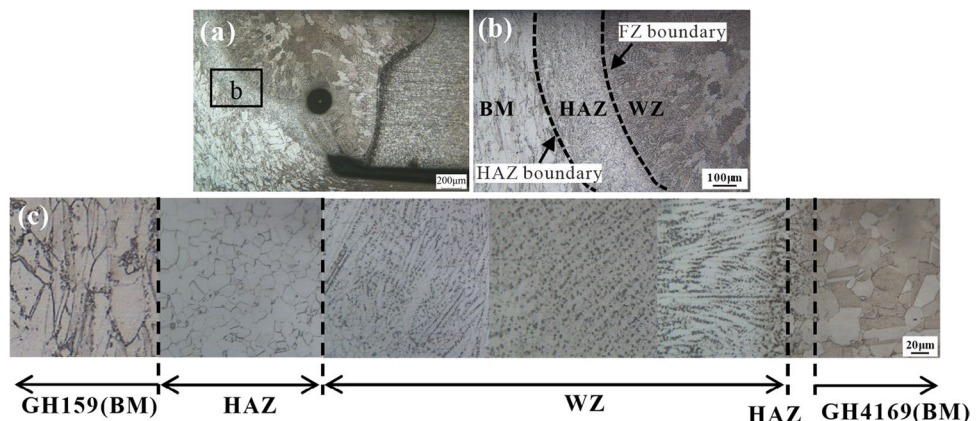

Fig. 3 The microhardness profiles of GH4169 and GH159 dissimilar joints under different aging time

Fig. 2 Microstructures of alloy joint: (**a**) The whole morphology; (**b**) Magnification of b in (**a**); (**c**) Magnification of (**a**)

Table 3 The average microhardness values at each zone in Fig. 3

Aging temperature T/℃	Holding time t/h	GH4169 (HV)	GH4169HAZ (HV)	WZ (HV)	GH159HAZ (HV)	GH159 (HV)
650	0	442.7	327.5	252.3	365.2	481.6
	25	451.2	433.4	396.0	468.6	520.5
	600	450.1	457.8	457.8	512.1	539.7
	2000	427.2	427.2	442.4	512.3	543

center area with the lowest hardness. The microhardness of unaged weldment (0 h) increases gradually from WZ to BM, and the post-weld aging treatment can greatly improve the microhardness of the weld center, making the microhardness distribution of each area of the weldment more uniform, resulting in a greatly improved service life of the joint. It can be seen from the microhardness-aging time curve that the microhardness of GH159BM increases with the aging time, while the microhardness of GH4169BM increases with the holding time within 25 h and gradually decreases after 25 h. According to previous research, GH4169 superalloy is a precipitate-strengthened nickel-based superalloy, and thus, the microhardness enhancement after aging treatment for 25 h mainly depends on the kind, volume fraction and size of precipitates [25].

The microhardness values of the WZ increase with aging time increasing. Especially at 25 h, the microhardness has the most significant enlargement, in which the value of microhardness was 396 HV about 144 HV higher in comparison with the unaged specimen. After the aging time is extended to 600 h, the microhardness gradually decreased. The WZ values are respectively 457.8 HV (600 h) and 442.4

HV (2000 h). Overall, the WZ was aged at 650 °C, and the microhardness increased rapidly with the aging time within 25 h. However, the increase rate of hardness decreased slowly from 25 to 600 h, and the microhardness value began to decline surpassing 600 h.

3.3 Chemical compositional change

The compositional changes in the weld joint with the unaged sample were microanalyzed by EDS through the weld line. EDS line scans of the main elements (Ni, Fe, Nb, Co, Mo, and Cr) are shown in Fig. 4. The content of elements in the transition region from the BM to the weld has a large gradient, and the elements diffuse from the BM to the center of the weld with uneven distribution. The Ni and Co at the joint are diffused from the base metal at both ends to the weld joint, following the principle of high concentration to low concentration diffusion. It can be observed from Fig. 4c and d that the content of Al and Fe does not change significantly, while Nb fluctuates significantly in HAZ and WZ. A small amount of Nb element contributes

Fig. 4 OM images of the welded joints: (**a**) GH159; (**b**) GH4169; (**c**), (**d**) are the distributions of elements across the fusion boundary in (**a**) and (**b**)
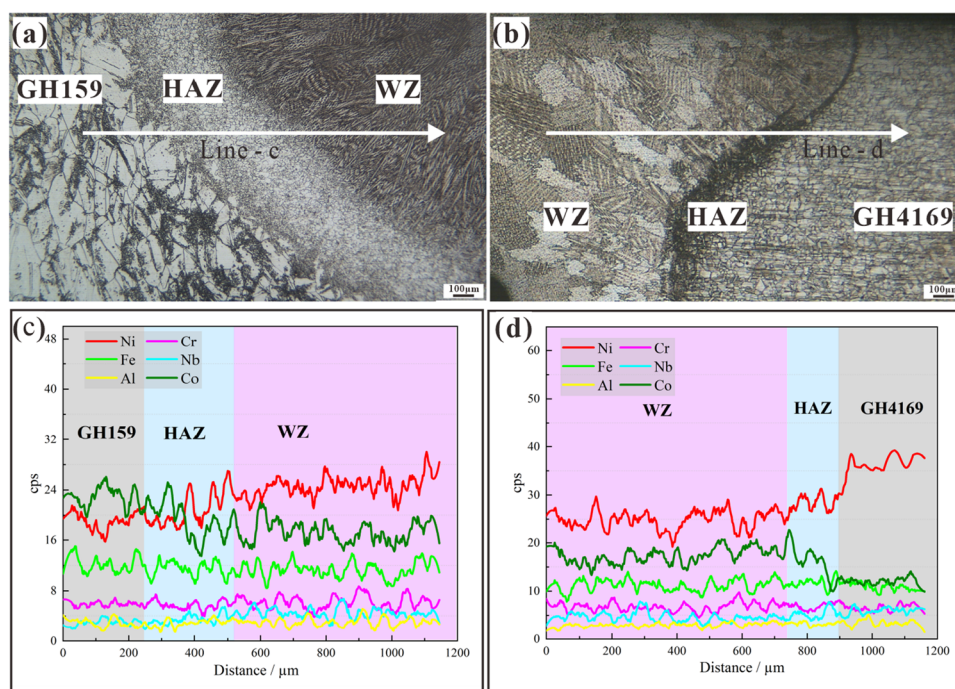
to stabilizing the austenitic microstructure, while Nb-enriched regions easily give rise to the appearance of MC-type carbides and precipitated phases [34].

Figure 5 shows the element distribution of GH159 super-alloy, fusion zone (FZ), and GH4169 superalloy in the joint from under different aging times. From the perspective of
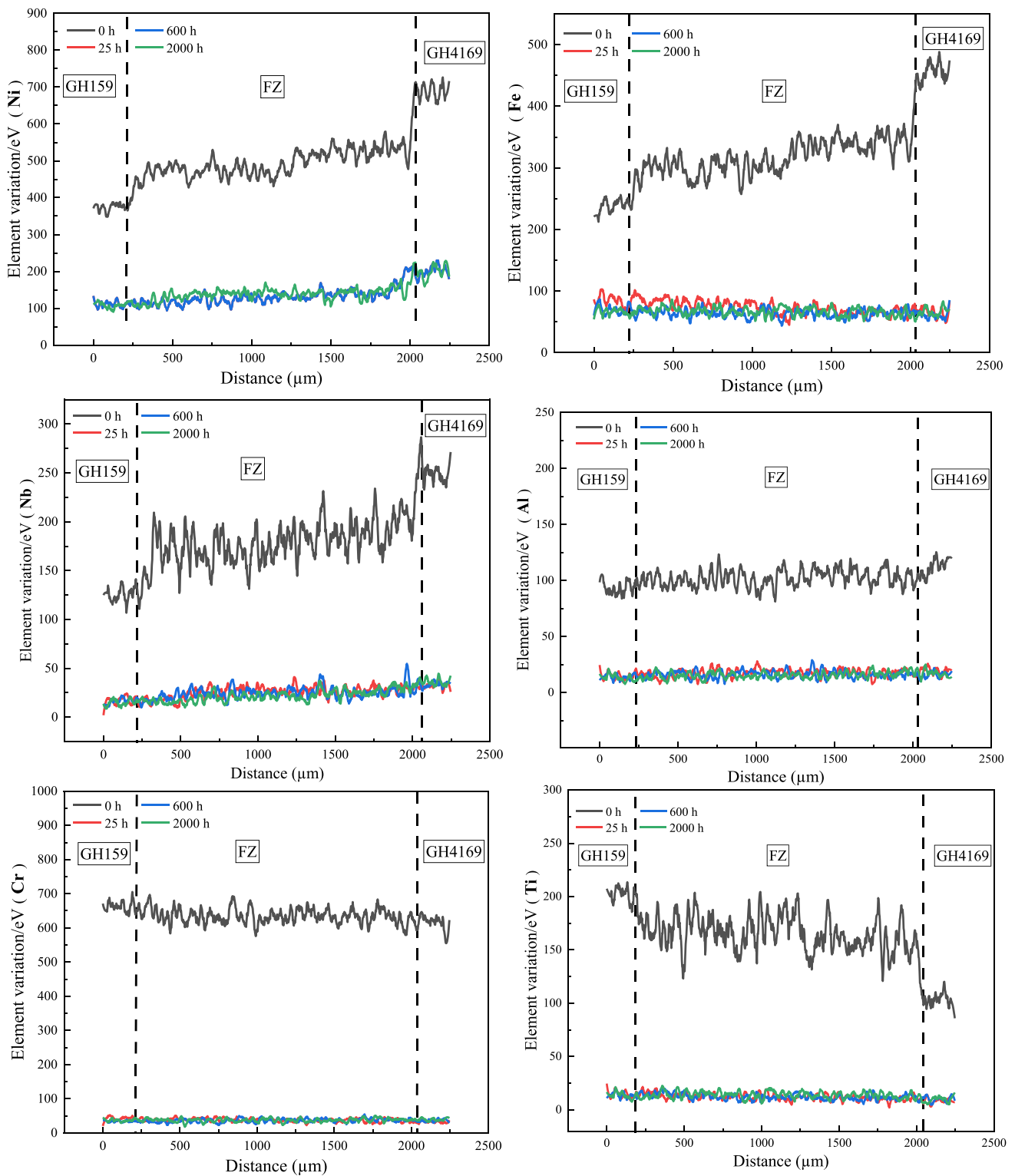

Fig. 5 Line scanning (EDS) of the welded joints

the overall element distribution, the element content fluctuates the closest to the fusion line, which means that the composition gradient on both sides is the largest and the most uneven. It is distinct that the content of Ni, Fe, and Nb reduced from GH4169BM to GH159BM side, while the content of Ti, Al, and Cr is almost unchanged. This is due to the transfer of atoms from high-content alloys to low-content alloys; the diffusion itself hinges on the intrinsic diffusion coefficient of each atom [29]. The Ni, Fe, and Nb are fully diffused and evenly distributed in all positions without segregation on aged at 25 h. In general, the aging treatment could effectively facilitate the diffusion of the elements and ease composition segregation. Besides, the element diffusion could alter the formation, distribution, and size of precipitates [35–37]. The effects of composition segregation on the precipitation of the second phase will be further studied in the following.

### 3.4 Microstructure of specimens before aging treatment

3.4.1 Base metals

Figure 6a exhibits the microstructure of GH159BM. It is seen that the microstructure of GH159BM consisted of some fine recrystallization grains formed at the grain boundaries of deformed grains (circle 1, corresponding magnification micrographs are shown in Fig. 6c), which resulted from hot pier processing before laser welding. Moreover, some coarse MC carbides were observed in the microstructure of GH159BM. These coarsened MC

carbides were confirmed as NbC by the EDS analysis (Fig. 6b). Figure 6d shows the TEM microstructure of GH159BM. Some fine second phases were visible, which was confirmed as TiC by the selected-area diffraction (SAD) (Fig. 6d and e). It is interesting to note that a large number of closely spaced intersecting networks were also found on the microstructure of GH159BM (Fig. 6d). It is seen from Fig. 3 that the microhardness of GH159BM is the highest in the weld joint of the GH159/GH4169 superalloy. The enhancement in the microhardness of GH159BM is mainly attributed to the appearance of a closely spaced intersecting network formed during cold drawn and fine TiC particles [16, 38–40].

Figure 7a and b illustrates the microstructure of equiaxed crystals and twins distributed in GH4169BM. SEM images result show that the blocky precipitate was confirmed to be NbC, and TEM images exhibited that nano-meter-size precipitates were observed in the GH4169BM (Fig. 7c). The SAD pattern of the sample along the $[001]\gamma$ direction is shown in Fig. 7d, where the red precipitates represent the γ' phase, while the yellow precipitates are expressed as γ'' phase with a body-centered tetragonal DO_{22} structure. The resulting dark field image using the diffraction spot marked by the red circle in Fig. 7d representing one family of γ' phases is given in Fig. 7e; and the morphology of γ'' phases are depicted Fig. 7f. It is generally known that the coherent strain between γ'' and matrix is higher and the γ'' phase usually presents with a disc-like shape, while the γ' phase, which has a low coherent strain with the matrix, is normally globular [5, 11].

Fig. 6 Microstructure of base metal GH159: (**a**)SEM image; (**b**) EDS diagram of NbC; (**c**) Recrystallization grains of arrow 1 in (**a**); (**d**) TiC carbide; (**e**) SAED of TiC carbide
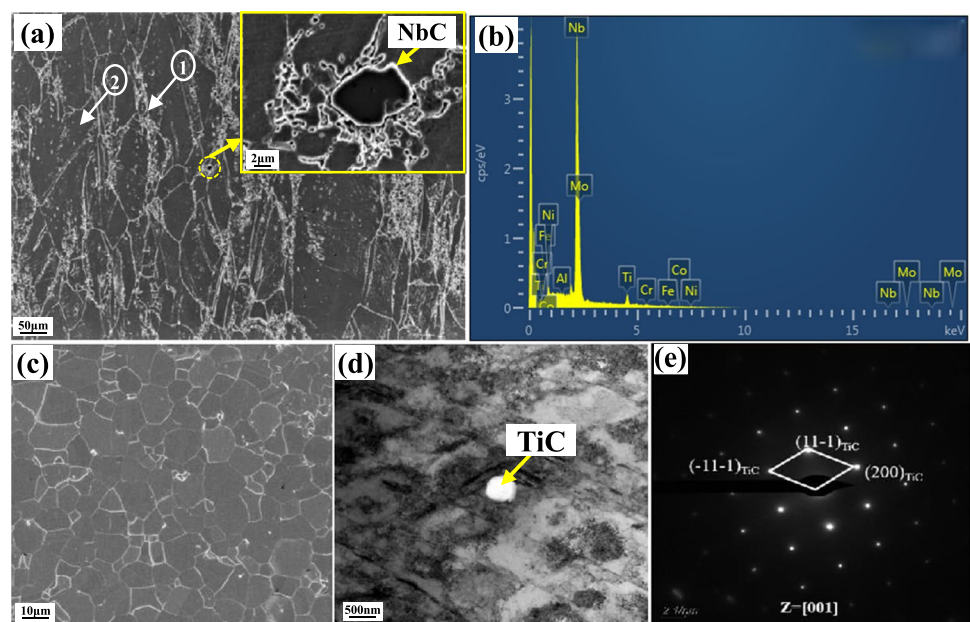
Fig. 7 Microstructure of base metal GH4169: (**a**) SEM image; (**b**) TEM image; (**c**) TEM BF image; (**d**) SAD pattern with the [001] zone axis indicating the coexistence of γ′ phase and γ″ phase within γ matrix; (**e**), (**f**) corresponding dark field images of γ′ phase and γ″ phase in (**d**)
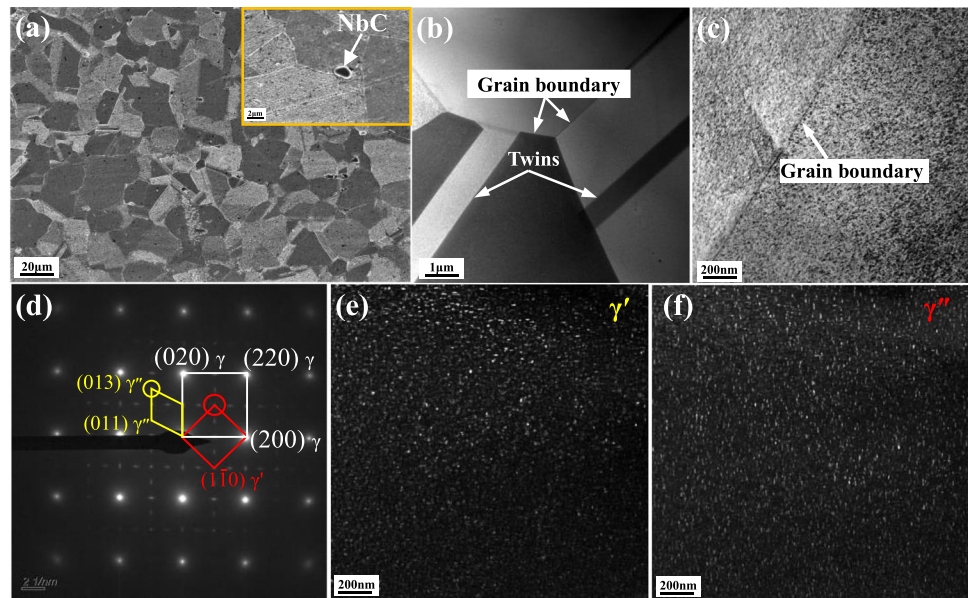
3.4.2 Phase compositions

Irregular-shaped precipitates can be observed in the center of the weld (Fig. 8), which show independent island-like, dendritic, and semi-continuous distributions with different sizes. Previous studies have shown that during the welding process of GH4169 superalloy, the redistribution of Nb and Ti will lead to the precipitation of topographically close-packed (TCP) phase, such as Laves (Fe, Ni, Cr)$_2$(Nb, Mo, Ti) (hexagonal) [41]. The Laves phase is a non-equilibrium eutectic product of L→γ+Laves that can be formed in the final solidification stage of the GH4169 superalloy [35, 37]. Figure 8c shows the electron diffraction pattern of the intergranular phase, which indicates that it has a hexagonal close-packed structure (HCP). Further EDS map analysis showed that this precipitated phase was enriched in Nb and Ti, and the contents of Ni and C were lower than those of γ matrix (as shown in Fig. 8d and e). The precipitated phase was identified as the Laves phase based on its structure and composition. The microhardness of the weldment unaged increased from the center of the weld to both sides. This is because the Laves phase consumes the strengthening element Nb, which reduces the weld strength, resulting in the lowest microhardness value of the weld center. The softening behavior of the Laves phase is consistent with that reported in the literature [1, 19].

3.5 Microstructure evolution of welded joints after aging treatment
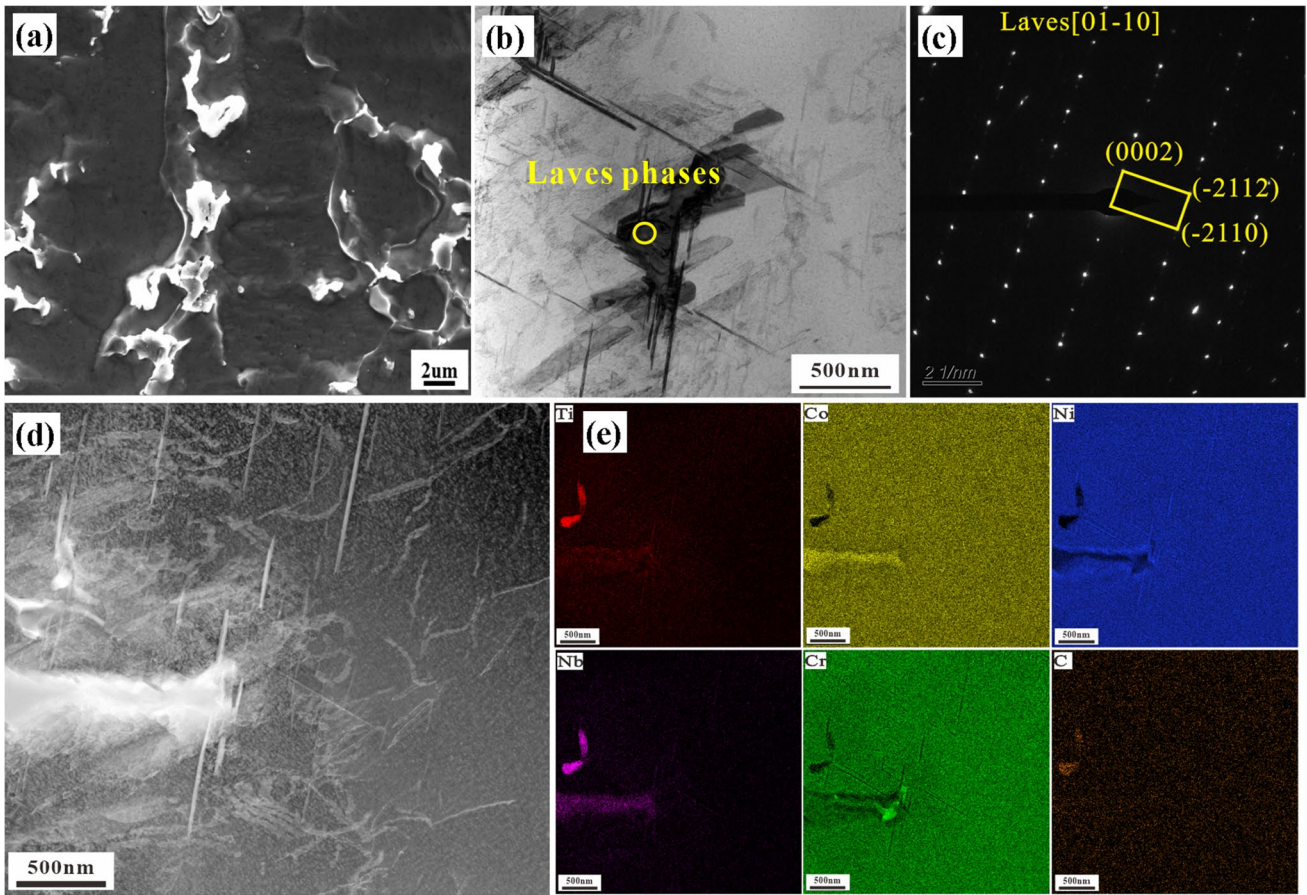
3.5.1 Microstructure of the BM

The microstructure of GH159BM under different aging treatments did not change significantly with the extension of aging time. However, the TEM image of Fig. 9a reveals that nano-precipitates appear in the matrix after aging treatment of GH159BM, and the SAD diagram shows that the nano-phase is the enhanced phase γ′. Figure 9b–d shows that the nano-meter γ′ phase is dispersed in γ matrix. The heat treatment temperature of GH159BM before welding is higher than the complete dissolution temperature of γ′ phase (910 °C), resulting in the disappearance of γ′ phase [42]. Therefore, there was no precipitation in the unaged sample. According to the statistics in Fig. 9e, the aging treatment is beneficial to the precipitation of γ′ phase, and the volume fraction and the size of γ′ phase increase with aging time. The phenomena suggest that the microhardness of GH159BM increases with aging time due to the amount of γ′ phase in the matrix increasing.

Figure 10 exhibits the morphology, size, and volume fraction of γ′ and γ″ phases in GH4169BM subjected to different aging treatments. The spherical γ′ phase has been observed in the matrix at aging 25 h; with continuous extending aging time, the γ′ phase continues to grow, and two or more fine particles are combined and finally grow into a strip γ′ phase (Fig. 10c and d). Similarly, the γ″ phase grows from an ellipsoidal shape to a thick strip with lengthening time, and the growth extends toward the two ends of the strip (Fig. 10e–h). The precipitated phases γ′ and γ″ are counted by IPP software, and the volume fraction and size of the strengthened phase are displayed in Fig. 10i and j. There is no significant difference in the average size of γ′ phase at aging for 0 h and 25 h with the mean diameter value of 1.6 ± 0.2 nm, and volume fractions are 4.0 ± 0.4% and 5.9 ± 0.3%, respectively. While the size of the γ′ phase increased from 40.8 nm (600 h) to 65.4 nm (2000 h), and the γ″ phase increased from 42.3 nm (600 h) to 104.1 nm (2000 h). This observation confirms that the

Fig. 8 (**a**) SEM image of microstructure of weld center; (**b**) TEM BF image; (**c**) SAED pattern taken from the corresponding marked area in (**b**); (**d**) HAADF image; (**e**) TEM mapping micrograph

Fig. 9 (**a**) SAD pattern with the [001] zone axis indicating the coexistence of γ′ phase within γ matrix; (**b**), (**c**) and (**d**) are γ′ phase dark field (DF) image of 25, 600 and 2000 h respectively; (**e**) The statistical results of average diameter and volume fraction of γ′ phase
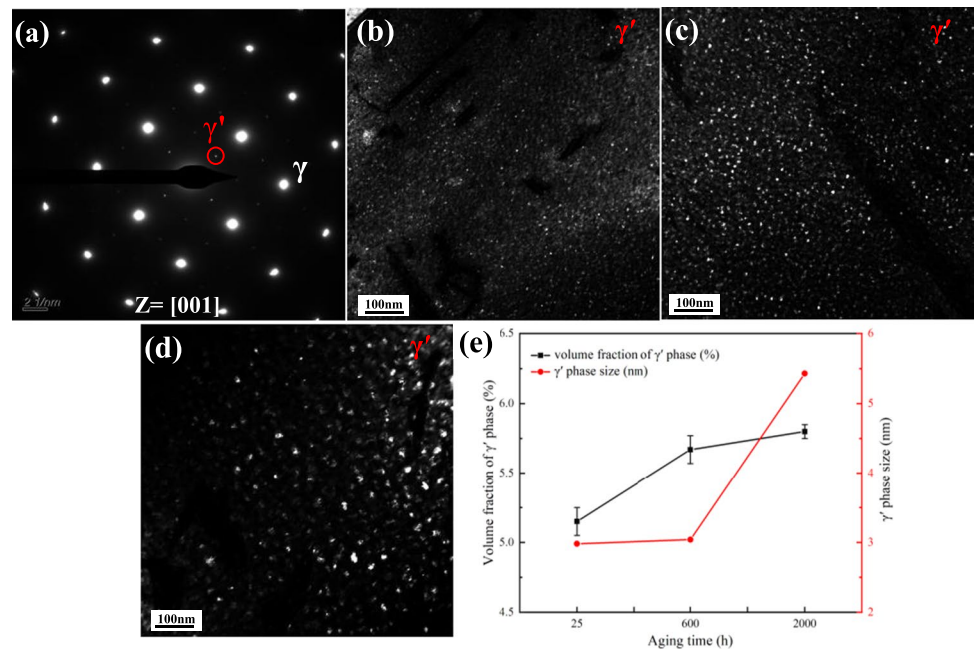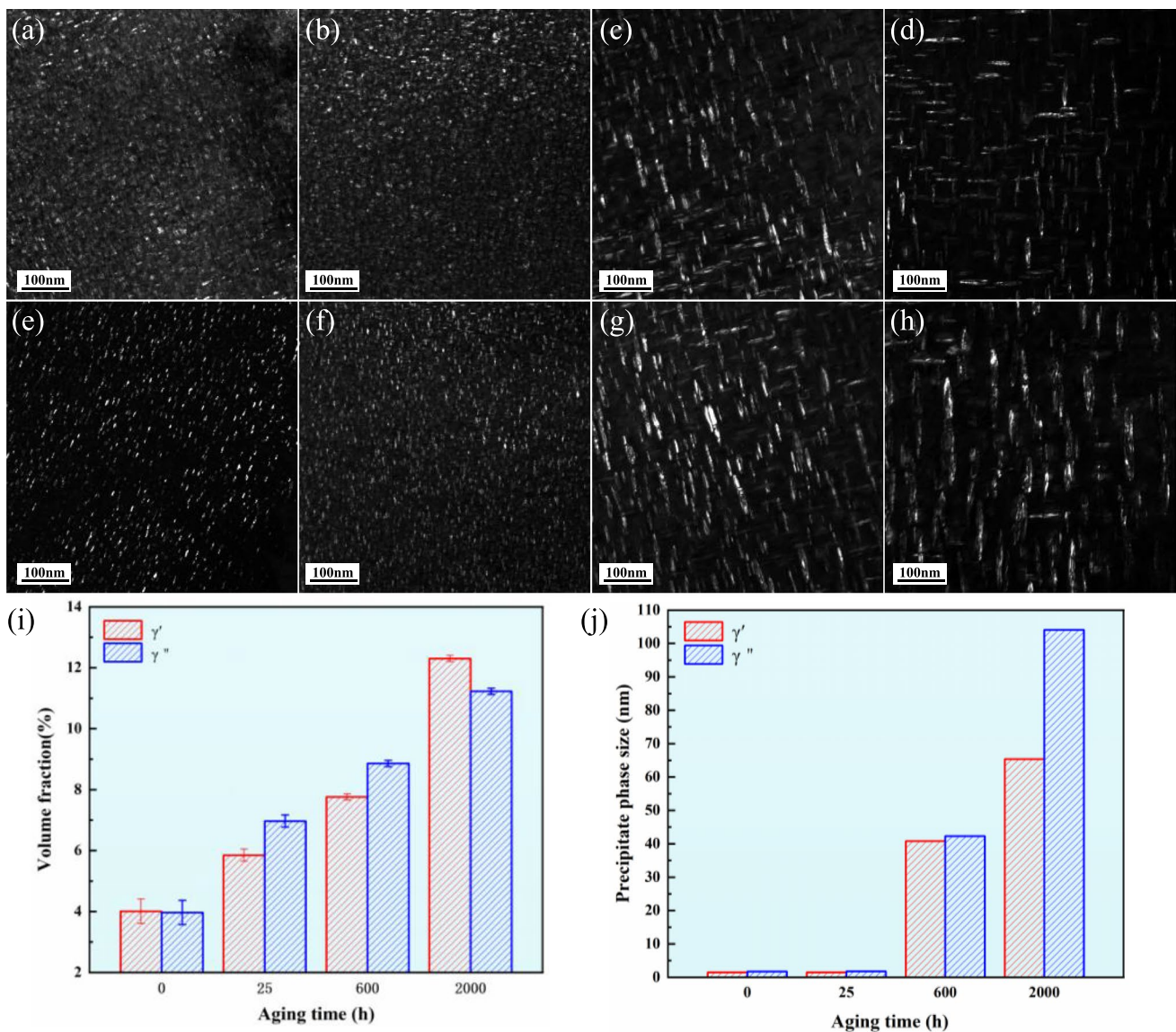
Fig. 10 TEM morphology of γ′ and γ″ phase of GH4169BM under different aging time: (**a-d**) γ′ phase for 0, 25, 600 and 2000 h respectively; (**e-h**) γ″ phase for 0, 25, 600 and 2000 h respectively; (**i**) and (**j**) are statistical results of volume fraction and average diameter of γ′ and γ″ phase

precipitates are constantly precipitated and grown during the long aging process. The growth of the main strengthening phase is controlled by the diffusion of Nb atoms, and the diffusion of elements is inevitably related to the temperature and time of aging treatment [43]. Therefore, the size of the precipitates can be controlled by regulating the aging treatment. The γ′ and γ″ phases have an excellent strengthening effect, and the microhardness increases with the increase of the number of precipitates within 25 h. However, the severe coarsening of the precipitated phase is caused by a long aging period [44, 45], which leads to a weakening of the strengthening effect and a consequent decrease in microhardness values (Fig. 3).

3.5.2 Dendrite

The sampling follows the principle that the BM zone, HAZ, WZ, and other areas of the weld are in the same plane. The sample is cut vertically from the center of the bolt and spring joint along the direction of the laser beam, and the sampling of different aging treatments strictly follows the same cutting mode. According to this principle, the morphology of dendritic tissues near the fusion line did not change significantly under different aging times. The dendrite arm spacing was measured by IPP software, and the relationship with aging time was depicted in Fig. 11. No significant difference

was observed in dendrite arm spacing within 25 h, while increased significantly when the aging time was extended to 600 h (4.72 μm) and 2000 h (5.42 μm), respectively. From this, it can be inferred that with the prolongation of aging time, the dendrites coarsen and the dendrite spacing increases. The dendrite arm spacing is a function of the cooling condition [19]. With increasing cooling rate, the dendrite arm spacing is decreased. In this present work, all samples were cooled to room temperature at the same cooling rate, and the effect of cooling rate on the dendrite arm spacing is the same. However, the dendrite arm spacing in this investigation is increased with increasing aging time. This indicates that the aging time also has a significant effect on the dendrite arm spacing. This may be attributed to the fact that the coarse dendrites formed first can exist stably, while the fine dendrites formed later will dissolve. The dissolution of fine dendrites results in an increase in the spacing of dendrite arms during long time aging.

From equation $HV = C + k\lambda^{-1/2}$ [46], where C and K are intrinsic constants of material and λ is dendrite arm spacing. According to the formula, the microhardness value is inversely proportional to the dendrite spacing. That is, the microhardness value increases with decreasing dendrite arm spacing. However, in this paper, with the extension of aging time, the dendrite arm spacing increases, while the microhardness of the weld area still increases (Fig. 3). Therefore, the difference in dendritic arm spacing after aging treatment has little effect on microhardness, and the precipitation phase plays the most important role and can overcome the softening effect of the material caused by the wide spacing of the dendrite arms.
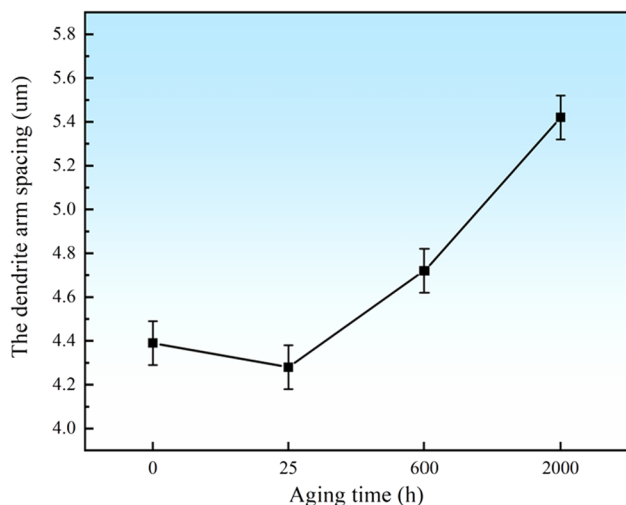
Fig. 11 The statistical results of dendrite arm spacing of joint with different aging time

### 3.5.3 Precipitate phase analysis of the WZ

Figure 12 depicts the evolution of the Laves phase on aged at 650 °C. The Laves phase particles in the weld without aging treatment are coarse and clustered into chained patterns in Fig. 12a, while they are semi-continuous on aging for 25 h. The sample aged 25 h offers better homogenization compared to the 0-h condition, as reflected in the more regular shape of Laves precipitates. The Laves phase distribution is highly interconnected in Fig. 12c with the aging time increasing. Figure 12e and f shows the curve of the volume fraction and average diameter of Laves phase changing with aging time. More than 25 h, the volume fraction of Laves phase increases with its coarsening after aging for a long period, and its morphology changes from the original chain structure to the network structure. The size and volume fraction of Laves phase obtained in the weld of 600 h are 0.95 μm and 27.35%, respectively. Upon increasing to 2000 h, the size of Laves phase decreased and the volume fraction of the Laves phase of the weld was only 19.59% (Fig. 12e). This is due to the presence of needle-like precipitates, which had a cutting effect on the Laves phase.

To identify such needle-like precipitates and their relationship to the matrix, a detailed TEM investigation is presented in Fig. 13. The inserted fast Fourier transformation (FFT) patterns verify that the needle-like precipitates were δ phases, which have an orthorhombic crystal structure, and the γ matrix has an FCC crystal structure in Fig. 13b. HRTEM micrograph exhibits the interface between the δ phase and the γ matrix, and the results of FFT show that the orientation relationship between the matrix and δ phase is $[011]_\gamma$ //$[100]_\delta$. This result is consistent with the proposition put forward by previous studies [47, 48]. Furthermore, a large-area γ′ phase could not be found in the aging-treated specimens during TEM observations, only a bit γ′ phase existed in the region away from the Laves phase, and the δ phase was precipitated around the Laves phase. Aging treatments at temperatures of 650 °C are insufficiently high to eliminate the microsegregation of Nb and Ti [43]. Once thermodynamic conditions permit, the acicular or rod-like δ phases will precipitate at grain boundaries that still retain enough Nb. When the aging time is extended to 2000 h, the Laves phase in the weld center is often used as the nucleation position of δ phase, and the remaining Nb around it promotes the nucleation and growth of δ phase [49].

The magnification SEM image of the microstructure of Laves phase aged at 650 °C is illustrated in Fig. 14, and the corresponding EDS analysis results are shown in Table 4. The content of Nb in Laves phase formed by WZ is only 8.68%, which is lower than 10%, thus resulting in an incomplete stable state of Laves phase [34, 35]. The low content of Nb in Laves phase during laser welding is attributed to a fast cooling speed, which results in not enough time for Nb

Fig. 12 SEM micrographs showing the microstructure in the center of weld pool for GH4169/GH159 samples with different aging time: (**a**) 0 h; (**b**) 25 h; (**c**) 600 h; (**d**) 2000 h;(**e**), (**f**) are statistical results of volume fraction and average diameter of Laves phases
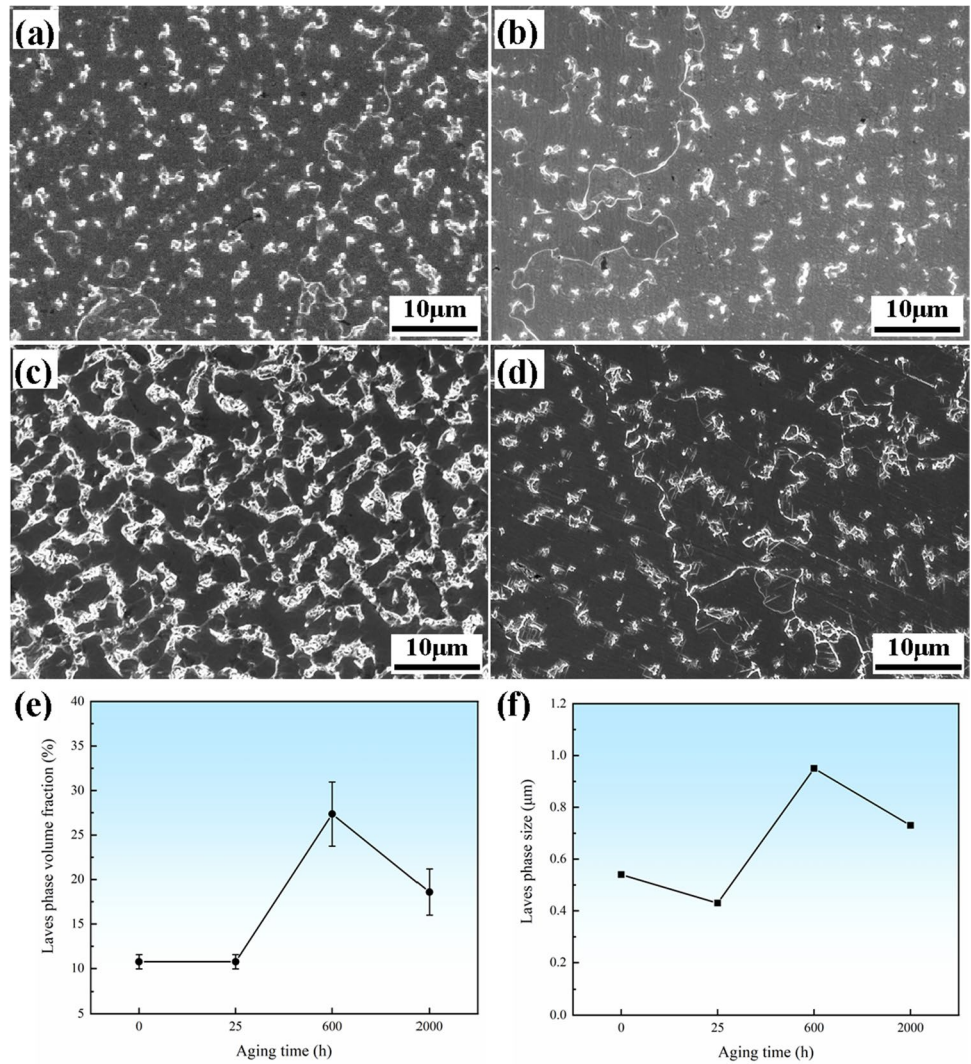
Fig. 13 (**a**) Bright-field TEM of the center of the weld joint aged at 650°C for 2000 h; (**b**) HRTEM micrograph of δ phase precipitating, superimposed with the FFT patterns of the image. Magnified atomic resolution TEM images of (**c**) the γ matrix along its [011] zone axis, (**d**) δ phase with an orthorhombic crystal structure examined from its [100] zone axis
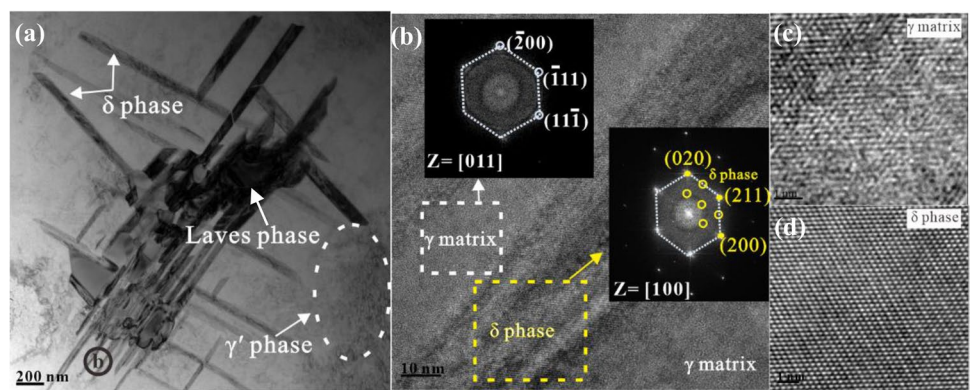

to fully diffuse and form a stable Laves phase. Therefore, the Laves phase was irregular and uneven in the samples after laser welding [8, 9]. During aging for 25 h, some unstable Laves phase will dissolve to the matrix and cause an increase in the content of Nb, whereas some other unstable

Laves phase distributed in the region with a high Nb content can transform to a stable Laves phase by obtaining Nb from the matrix [34], as shown in Fig. 12e and f. With increasing aging time to 600 h, the stable Laves phase gradually grow to 0.95 μm and the volume fraction of Laves phase

Fig. 14 SEM micrographs of the Laves phase at different aging time: (**a**) 0 h; (**b**) 25 h; (**c**) 600 h; (**d**) 2000 h
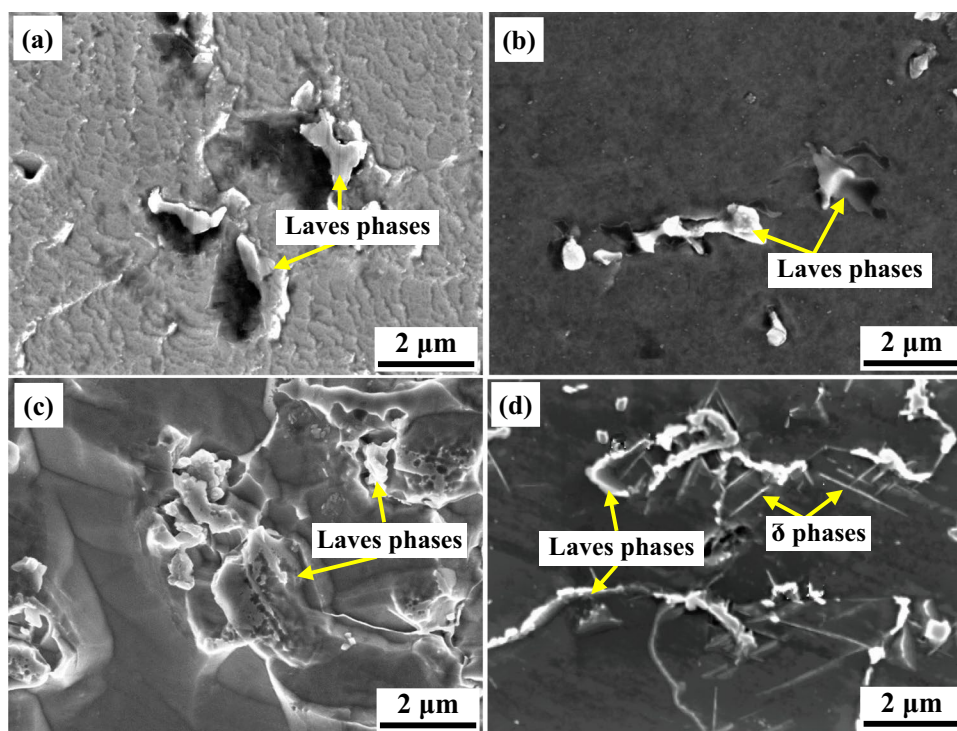
Table 4 Energy spectrum analysis of Laves phase and mataix (wt %)

|	Aging time (h)	Ni	Nb	Ti	Cr	Mo	Co	Fe
Laves	0	32.95	8.68	3.16	14.78	6.89	16.73	11.0
	25	27.03	12.45	2.32	13.07	7.38	8.47	11.29
	600	29.18	12.87	2.57	14.22	10.04	13.09	9.69
	2000	21.85	12.05	3.21	22.3	12.39	18.2	9.8
Matrix	/	46.16	2.16	1.89	17.53	3.11	7.2	17.76

was measured to be approximately 27.35%. It was noted that the volume fraction of the Laves phase decreased to 19.59% after aging treatment for 2000 h. This is attributed to the formation of a large number of needle-like δ phases around the Laves phase, which results in a decrease in the content of Nb in Laves phase, and thick Laves phase is cut into fragments [50, 51]. Some of the fragments of Laves phase will dissolve into the matrix during aging, leading to a decrease in the volume fraction of the Laves phase.

Figure 15 displays the microstructure of the weld center analyzed by TEM. From the bright-field image, the nanophase distributed in the Laves phase interval region can be observed, and the γ′ phase exists in the matrix by calibrating the diffraction pattern. Dark-field image of the γ′ phase (Fig. 15c) is marked by the red circle in (b). Since the presence of Laves phase consumes Nb and suppresses the nucleation of γ″ phase, the presence of γ″ phase is not detected. Therefore, the γ′ phase in the center of the weld plays a major strengthening role. Figure 15c–e shows the γ′ phase distribution at the weld center at the different aging times of

25, 600, and 2000 h, respectively. The γ′ phase precipitation is spherical, and the distribution is fine and uniform within 25 h. A clear increase in the overall size of the precipitates is seen as the aging time reaches 2000 h in Fig. 15e. In contrast, γ′ phase in GH4169BM grew from spherical to a long strip after long-term aging treatment, and γ′ phase in the weld center was still spherical after aging for 2000 h. This is because Laves phase is evenly distributed in the center of the weld, γ′ phase can only precipitate in the Laves phase gap, and its growth is hindered by Laves in the aging process. Therefore, the final morphology is still spherical.

Microhardness is the result of the joint effect of grain refinement degree and dissolution or transformation of the strengthening phase [45]. No γ′ and γ″ phases were observed in the unaged sample, which attributes to the characteristics of LBW with high temperature and cooling speed [52, 53]. The γ′ and γ″ phases in the BM dissolve during the welding process, while there is not enough time to precipitate during the solidification process. In addition, the irregular and uneven distribution of Laves phase

Fig. 15 TEM photograph of weld pool center of GH4169/GH159 welding joint: (**a**) bright field image aged at 650∘C for 25 h; (**b**) SAD diagram with the [001] zone axis, indicating that γ′ phase exists in γ matrix; (**c**) the dark field image corresponds to the γ′ phase marked by the red circle in (**b**); (**d**) 600 h; (**e**) 2000 h
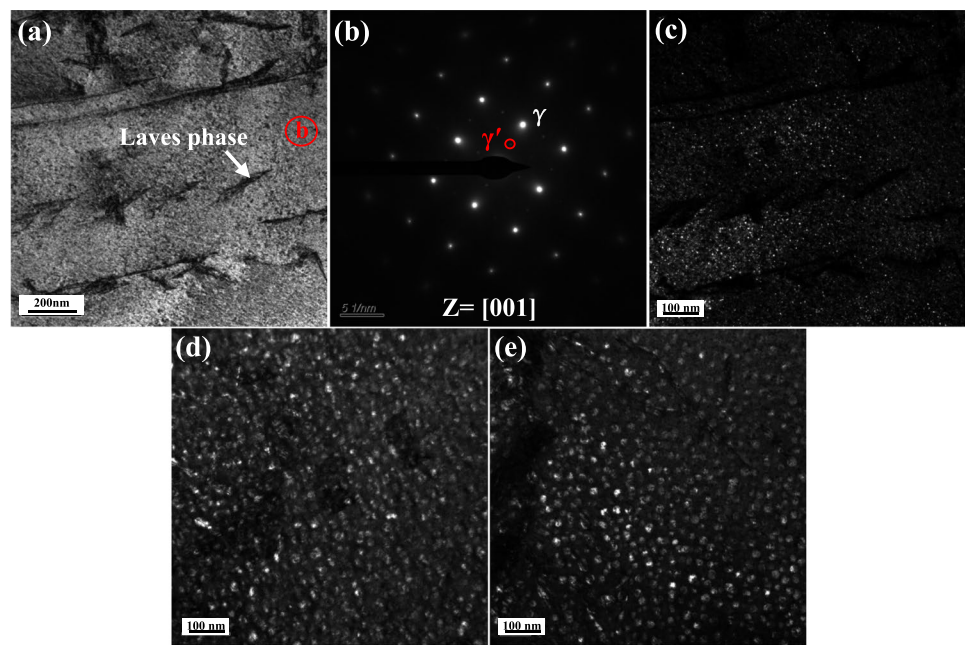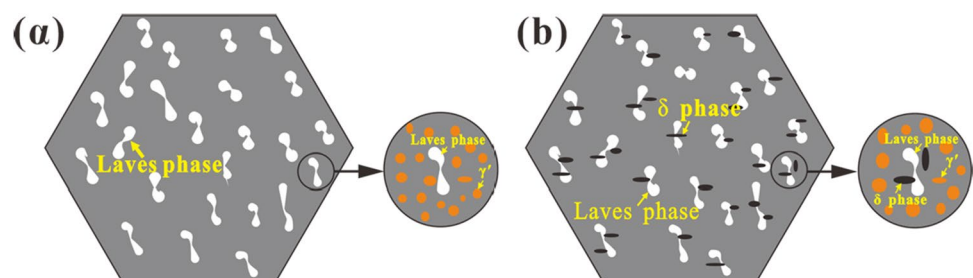
resulted in the lowest microhardness of the unaged sample (as shown in Fig. 12). After aging for 25 h, the microhardness has a significant increment, which is attributed to a fact that the aging treatment promoted the diffusion of elements, improved the distribution of Laves phase, and precipitated the strengthened phases γ′ and γ″ [54]. It can effectively improve the weld microhardness and bring broad application prospects for welding products. However, the precipitated phase grows with the extension of aging time. Especially, after aging for 600 h, both the strengthening phase and the Laves phase in the weld have severe coarsening, which results in a slow increase in microhardness. It is worth noting that the WZ had a more obvious increasing trend compared with the BM and the HAZ in Fig. 3, which can be attributed to the existence of the Laves phase which can hinder the coarsening of the strengthening γ′ phase. After aging for 2000 h, the microhardness of WZ sample is slightly lower than that of 600 h. This has been caused by the δ phase precipitated along the boundary of Laves phase, which consumes Nb and inhibits precipitation of the strengthening phase, eventually leading to the decrease of the microhardness [51].

The schematic illustration of the microstructure in the WZ at 650 °C for different holding times is shown in Fig. 16. After the welding, there is a uniform Laves phase in the center of the weld, which gradually coarsens with the extension of aging time. Furthermore, nano-phase γ′ is precipitated in the matrix, which grows spherically due to the obstruction of Laves. At 2000 h, the γ′ phase exists only in the region far from Laves, while it is not observed in the region near Laves. It was confirmed that Nb was consumed due to the precipitation of δ phase around Laves; therefore, the precipitation of strengthened phase γ′ is reduced. The reason is that the δ phase tends to nucleate preferentially at the interface of Laves phase because of the large distortion energy in the region around Laves phase.

4 Conclusions

In this paper, Laser beam welding is used for dissimilar welding of GH159/GH4169 superalloys. The effect of postweld aging treatment on weld microstructure and microhardness is studied. Main conclusions can be drawn as follows:

Fig. 16 Schematic illustration of the microstructure in the center of weld pool at different time of 650∘C aging treatment: (**a**) 600 h; (**b**) 2000 h

1. A non-uniform distribution of composition and microhardness was observed based on the large difference between BM and WZ. The WZ of the joint has the lowest microhardness and is often the weakest link of the welding parts. The WZ microhardness increases by 144HV after aging for 25 h, and the microhardness is the result of the joint effect of grain refinement degree and dissolution or transformation of the strengthening phase.

2. The post-weld aging treatment effectively alleviates the serious problem of alloying element segregation in welded joints. It can promote the full diffusion of elements to form a stable microstructure and improve the uneven distribution of the precipitated phase.

3. With the extension of aging time, the volume fraction and size of nano-phase γ' and γ'' in the matrix increased. Owing to the precipitated phase with fine dispersion distribution having a higher hardening effect, the short-term aging hardness increases significantly, while long-term aging time leads to severe coarsening of the strengthened phase, resulting in a reduction in microhardness.

4. On aged 650 °C for 2000 h, the δ phase precipitates at Laves interface can promote the dissolution of Laves phase. The volume fraction and size of Laves phase in the samples aged for 2000 h decreased significantly compared with 600 h. It is similar to the Laves phase being "cut" by the δ phase from a long strip shape to a large granular shape.

Data Availability All data that support the findings of this study are included within the article (and any supplementary files).

Declarations

Conflict of interest The authors declare no competing interests.

References

1. Sonar T, Balasubramanian V, Malarvizhi S, Venkateswaran T, Sivakumar D (2021) An overview on welding of Inconel 718 alloy - effect of welding processes on microstructural evolution and mechanical properties of joints. Mater Charact. 110997

2. Li Y, Luo Z, Liu J, Ma H, Yang D (2021) Dynamic modeling and stability analysis of a rotor-bearing system with bolted-disk joint. Mech Syst Signal Pr 158:107778

3. Zou C, Xia H, Chen K, Zhai J, Han Q (2022) Research on the identification method of the pre-tightening state of the matching surface of the aero-engine disk-drum rotor. Eng Fail Anal 136:106208

4. Luo L, Ru Y, Ma Y, Li S, Gong S (2022) Design for 1200°C creep properties of Ni-based single crystal superalloys: effect of γ'-forming elements and its microscopic mechanism. Mater Sci Eng A 832:142494

5. Liu H, Guo K, Sun J, Shi H (2022) Effect of Nb addition on the microstructure and mechanical properties of Inconel 718 fabricated by laser directed energy deposition. Mater Charact 183:111601

6. Zhao Z, Qian N, Ding W, Wang Y, Fu Y (2020) Profile grinding of DZ125 nickel-based superalloy: grinding heat, temperature field, and surface quality. J Manuf Process 57:10–22

7. Yang J, Liu D, Zhang X, Liu M, Zhao W, Liu C (2020) The effect of ultrasonic surface rolling process on the fretting fatigue property of GH4169 superalloy. Int J Fatigue 133:105373

8. Cheng H, Kang L, Pang J, Xue B, Du D, Chang B (2021) Effect of the welding position on weld quality when laser welding Inconel 617 Ni-based superalloy. Opt Laser Technol 139:106962

9. Wang L, Huang Y, Yang D, Li H, Peng Y, Wang K (2020) Multi-scale simulation of grain growth during laser beam welding of nickel-based superalloy. J Mater Res Technol 9:15034–15044

10. Saju T, Velu M (2021) Review on welding and fracture of nickel based superalloys. Mate Today: Proc 46:7161–7169

11. Huang L, Cao Y, Zhang J, Gao X, Li G, Wang Y (2021) Effect of heat treatment on the microstructure evolution and mechanical behaviour of a selective laser melted Inconel 718 alloy. J Alloys Compd 865:158613

12. Qin H, Bi Z, Yu H, Feng G, Du J, Zhang J (2018) Influence of stress on γ'' precipitation behavior in Inconel 718 during aging. J Alloys Compd. S1511894638

13. Cazic I, Zollinger J, Mathieu S, El Kandaoui M, Plapper P, Appolaire B (2021) New insights into the origin of fine equiaxed microstructures in additively manufactured Inconel 718. Scripta Mater 195:113740

14. Han GW, Jones IP, Smallman RE (2003) Direct evidence for Suzuki segregation and Cottrell pinning in MP159 superalloy obtained by FEG(S)TEM/EDX. Acta Mater 51:2731–2742

15. Shiqiang L, Baozhong S, Zijian L, Renhui W, Fangchang Z (2002) Hardening mechanism of MP159 alloy induced by aging, T Nnonferr Metal Soc. 256–259

16. Gu J, Guo L, Gan B, Bi Z, Song M (2021) Microstructure and mechanical properties of an MP159 alloy processed by torsional deformation and subsequent annealing. Mater Sci Eng A. 802

17. Zhang WW, Yang Y, Tan YB, Zeng MT, Ma M, Xiang S, Zhao F (2022) Microstructure evolution and strengthening mechanisms of MP159 superalloy during room temperature rolling and cryorolling. J Alloys Compd 908:164667

18. Zhang Y, Yu J, Lin X, Guo P, Yu X, Zhang S, Liu J, Huang W (2022) Passive behavior of laser directed energy deposited Inconel 718 after homogenization and aging heat treatment. Corros Sci 205:110439

19. Ran Q, Xiang S, Tan Y, Hu S (2021) Effect of heat input on microstructure and mechanical properties of GH159 and GH4169 dissimilar joints by laser beam welding. Mater Res Express

20. Cao X, Rivaux B, Jahazi M, Cuddy J, Birur A (2009) Effect of pre- and post-weld heat treatment on metallurgical and tensile properties of Inconel 718 alloy butt joints welded using 4 kW Nd:YAG laser. J Mater Sci 44:4557–4571

21. Yu K, Jiang Z, Leng B, Li C, Chen S, Tao W, Zhou X, Li Z (2016) Effects of post-weld heat treatment on microstructure and mechanical properties of laser welds in GH3535 superalloy. Opt Laser Technol 81:18–25

22. Bae SH, Kwon SI, Yoon JG (2014) Effect of post weld heat treatment on cryogenic mechanical properties of electron beam welded cast Inconel 718. Metall Mater Trans A

23. Wang W, Jiang L, Li C, Leng B, Ye X, Liu R, Chen S, Yu K, Li Z, Zhou X (2019) Effects of post-weld heat treatment on

microstructure and mechanical properties of Hastelloy N super-alloy welds. Mater Today Commun 19:230–237

24. Raghavan S, Zhang B, Wang P, Sun CN, Nai MLS, Li T, Wei J (2016) Effect of different heat treatments on the microstructure and mechanical properties in selective laser melted INCONEL 718 alloy, Mater Manuf Process. 10422016–10426914

25. Wang W, Chen Z, Lu W, Meng F, Zhao T (2022) Heat treatment for selective laser melting of Inconel 718 alloy with simultaneously enhanced tensile strength and fatigue properties, J. Alloys. Compd. 913

26. Zhou L, Xu P, Lin T, Zhu X, Liang Y, Liang Y (2022) Outstanding ductility of flash-butt welded Inconel 718 joints after post-weld heat treatment. Mater Sci Eng A 843:143132

27. Damodaram R, Raman S, Rao KP (2014) Effect of post-weld heat treatments on microstructure and mechanical properties of friction welded alloy 718 joints. Mater Des 53:954–961

28. Kuo TY, Jeng SL (2005) Porosity reduction in Nd–YAG laser welding of stainless steel and inconel alloy by using a pulsed wave. J Phys D 38:722

29. St A, Ra B, Bcdf C, Mj A (2021) Dissimilar linear friction welding of selective laser melted Inconel 718 to forged Ni-based superalloy AD730 TM: evolution of strengthening phases. J Mater Sci Technol

30. Thejasree P, Krishnamachary PC (2022) Weldability analysis and ANFIS modelling on laser welding of Inconel 718 thin sheets. Mater Manuf Process 37:1190–1202

31. Sharma SK, Biswas K, Nath AK, Manna I, Dutta Majumdar J (2020) Microstructural change during laser welding of Inconel 718. Optick 218:165029

32. Ram G, Reddy AV, Rao KP, Reddy GM, Sundar J (2005) Microstructure and tensile properties of Inconel 718 pulsed Nd-YAG laser welds. J Mater Process Tech 167:73–82

33 NaffakhMoosavy H, Aboutalebi M, Seyedein SH, Mapelli C (2013) Microstructural, mechanical and weldability assessments of the dissimilar welds between γ′- and γ″-strengthened nickel-base superalloys. Mater Charact 82:41–49

34. Liu F, Lyu F, Liu F, Lin X, Huang C (2020) Laves phase control of inconel 718 superalloy fabricated by laser direct energy deposition via δ aging and solution treatment. J Mater Res Technol 9:9753–9765

35. Kang M, Han Y, Zhou W, Shu Da, Gao H (2015) Study of microsegregation and Laves phase in INCONEL718 superalloy regarding cooling rate during solidification. J Mater Process Tech A 46:354–361

36. Yu X, Lin X, Liu F, Wang L, Tang Y, Li J, Zhang S, Huang W (2020) Influence of post-heat-treatment on the microstructure and fracture toughness properties of Inconel 718 fabricated with laser directed energy deposition additive manufacturing. Mater Sci Eng A 798:140092

37. Xiao H, Li SM, Xiao WJ, Li YQ, Cha LM, Mazumder J, Song LJ (2017) Effects of laser modes on Nb segregation and Laves phase formation during laser additive manufacturing of nickel-based superalloy. Mater Lett 188:260–262

38. Slaney JS, Nebiolo RA (1983) Development of multiphase alloy MP159 using experimental statistics. Metallogr 16:137–160

39. Shiqiang L, Baozhong S, Zijian L, Renhui W, Fangchang Z (2000) Investigation on the cold deformation strengthening mechanism in MP159 alloy. Metall Mater Trans A

40. Wilson JM, Shin YC (2012) Microstructure and wear properties of laser-deposited functionally graded Inconel 690 reinforced with TiC. Surf Coat Technol 207:517–522

41. Dupont JN, Lippold JC, Kiser SD (2011) Welding metallurgy and weldability of nickel-base alloys. Wiley, Hoboken, New Jersey

42. Zhang W, Yang Y, Tan Y, Xiang S, Shi W, Ma M (2022) Hot corrosion behavior and mechanism of cryo-rolled MP159 superalloy with long rod-like γ′ phase. Corros Sci 209:110706

43. Davies C, Nash P, Stevens RN (1980) The effect of volume fraction of precipitate on Ostwald ripening. Acta Metall 28:179–189

44. Zhang H, Hao H, Li J, Zhang X, Liu Y (2023) Evaluation on static mechanical stability of wrought Inconel 718 superalloy; effect of grain configuration and δ precipitation. J Mater Res Technol

45. Geng P, Qin G, Li T, Zhou J, Zou Z, Yang F (2019) Microstructural characterization and mechanical property of GH4169 superalloy joints obtained by linear friction welding. J Manuf Process 45:100–114

46 Ye RR, Li HY, Ding RG, Doel T, Bowen P (2020) Microstructure and microhardness of dissimilar weldment of Ni-based superalloys IN718-IN713LC. Mater Sci Eng A 774:138894

47. Chen MS, Zou ZH, Lin YC, Li HB, Yuan WQ (2018) Effects of annealing parameters on microstructural evolution of a typical nickel-based superalloy during annealing treatment. Mater Charact 14:212–222

48. Rafiei M, Mirzadeh H, Malekan M (2019) Micro-mechanisms and precipitation kinetics of delta (δ) phase in Inconel 718 superalloy during aging - ScienceDirect. J Alloys Compd 795:207–212

49. Kruk A, Cempura G (2023) Decomposition of the Laves phase in the fusion zone of the Inconel 718/ATI 718Plus® welded joint during isothermal holding at a temperature of 649°C. Mater Charact 196:112560

50. Hui X, Li S, Xu H, Mazumder J, Song L (2017) Laves phase control of Inconel 718 alloy using quasi-continuous-wave laser additive manufacturing. Mater Des 122:330–339

51. Stegman B, Yang B, Shang Z, Ding J, Sun T, Lopez J, Jarosinski W, Wang H, Zhang X (2022) Reactive introduction of oxide nanoparticles in additively manufactured 718 Ni alloys with improved high temperature performance. J Alloys Compd 920:165846

52. Madhankumar S, Ashwin S, Robert JA, Francis JC, Anton WJ (2021) Experimental investigation on ultimate tensile strength of laser butt welded inconel 718 alloy and 2205 duplex stainless steel. Mater Today: Proc

53. Ramkumar KD, Dev S, Phani PKV, Rajendran R, Narayanan S (2019) Microstructure and properties of Inconel 718 and AISI 416 laser welded joints. J Mater Process Tech 266:52–62

54. Shi JJ, Zhou SA, Chen HH, Cao GH, Chen GF (2020) Microstructure and creep anisotropy of Inconel 718 alloy processed by selective laser melting. Mater Sci Eng A 805:140583